33RD CONGRESS
OF THE INTERNATIONAL COUNCIL
OF THE AERONAUTICAL SCIENCES
STOCKHOLM, SWEDEN, 4-9 SEPTEMBER, 2022

ICAS 2022 SWEDEN

Unsteady Turbulent Flow Simulation of Rotor Blades on Moving Cartesian Grids Using Recursive Fitting Approach

Keisuke Sugaya[1], & Taro Imamura[1]

[1]The University of Tokyo, Tokyo, 113-8656, Japan

Abstract

To simulate turbulent flow around moving bodies, we propose a new method capable of automatic grid generation and accurate turbulent flow simulation in two- and three-dimension. The recursive fitting method (RFM) based on the Cartesian grid method is employed for the automatic body-fitted grid generation. Since the automatically generated body-fitted grids are used, near-wall treatment becomes straightforward in flow simulation. Further, the coupling of the RFM with the moving grid method allows the flow around moving bodies, such as electric fans and rotor blades, to be simulated. The grid moves with the body surface; thus, spurious pressure oscillations do not occur. To examine the capability of the proposed method, two- and three-dimensional flow simulations are conducted. Results show that the RFM simulation agrees well with the experimental data and those of simulation on conventional body-fitted grids.

Keywords: Cartesian Grid Methods, Computational Fluid Dynamics, Rotor Blades, Turbulent Flow.

Nomenclature

a_∞	Sonic speed
C_p	Surface pressure coefficient, $C_p = (p - p_\infty)/\left(\rho_\infty a_\infty^2 M_{tip}^2 (r/R)^2/2\right)$
C_Q	Torque coefficient, $C_Q = Q/\left(\pi R^3 \rho_\infty a_\infty^2 M_{tip}\right)$
C_T	Thrust coefficient, $C_T = F_T/\left(\pi R^2 \rho_\infty a_\infty^2 M_{tip}\right)$
F_T	Thrust
FM	Figure of Merit, $FM = C_T^{3/2}/(\sqrt{2}\, C_Q)$
M_{tip}	Tip Mach number, $M_{tip} = \Omega R/a_\infty$
Q	Torque
R	Radius of rotor
Ω	Angular velocity

1. Introduction

To achieve the green transformation, the development of eco-friendly aircraft is crucial. Thus, hybrid-electric aircraft with distributed electric fans have been studied [1]. Meanwhile, urban air mobilities capable of vertical take-off and landing using the rotors are attracting attention as a new transportation system. Unlike conventional aircraft, little or no statistical and empirical knowledge exist for designing these innovative aircraft; therefore, high fidelity performance evaluation using Computational Fluid Dynamics (CFD) based on the Navier–Stokes equations is essential. CFD has been used to predict the aerodynamic performance of conventional fixed-wing aircraft in the field of aeronautical engineering. To utilize CFD for designing innovative flying vehicles, further development of numerical methods for unsteady flow simulation around moving bodies is necessary.

To simulate the flow around electric fans and rotor blades, two methods are widely used: the fixed grid method [2-6] and the moving grid method [7-10]. In the fixed grid method, non-body-fitted grids fixed in space, such as Cartesian grids, are generated first. Then, moving bodies are tracked in a Lagrangian fashion. Level-set methods [11] are widely used to represent the body surface and its

motion. To simulate the flow near body surfaces, immersed boundary methods (IBMs) [2-5] or cut-cell methods [6] combine with the fixed grid method. The fixed grid method is widely used to simulate the flow around the moving bodies. However, the application of this method to turbulent flow is challenging since the turbulent boundary layer sweeping through the cells along with the body motion needs to be simulated. Further, difficulties arise when a cell inside the body at one moment becomes a fluid cell at the next time step. This is the so-called “fresh cell” problem, and the generation of spurious pressure oscillations has been reported [3,4].

Meanwhile, a grid moves with a body in the moving grid method. Conventional body-fitted grids are generally used [7,8]. The generation of body-fitted grids around complex geometries is a bottleneck in the CFD workflow since human intervention is required [12]. To overcome this problem, combinations of the moving grid method and IBMs are recently attracting attention [9,10]. Since non-body-fitted Cartesian grids are used, the grid can be generated automatically. However, the flow near the body surface needs to be interpolated from the surrounding flow since the flow is simulated on non-body-fitted grids. Thus, simulation results sometimes depend on the location of the “image point,” which is used for interpolation.

Recently, the recursive fitting method (RFM) based on Cartesian grid methods has been proposed to simulate a three-dimensional (3D) flow of fixed-wing aircraft [13,14]. This method is based on the simplified cut-cell method proposed by Harada et al. [15,16]. The RFM is capable of automatic grid generation around 3D geometries while the flow is simulated on the automatically generated body-fitted grids. Compared with IBMs on non-body-fitted Cartesian grids, the near-wall treatment becomes straightforward in flow simulation since the same wall boundary conditions as the conventional body-fitted grid can be used.

In this study, we proposed a new method capable of automatic grid generation and accurate turbulent flow simulation around two-dimensional (2D) and 3D moving bodies. The RFM combines with the moving grid method; thus, the automatically generated body-fitted Cartesian grids move following body motion. The near-wall treatment becomes straightforward in the RFM flow simulation, as opposed to the IBM. Further, the “fresh cell” problem does not occur since the grid moves with the body surface. The solver used in this study is developed based on the hierarchical Cartesian-grid-based grid generator and flow solver: the University of Tokyo Cartesian-grid-based automatic flow solver (UTCart) [17,18]. To examine the proposed method, 2D and 3D unsteady turbulent flow simulations around moving bodies are conducted. First, the 2D Reynolds averaged Navier–Stokes (RANS) simulation around the pitching airfoil is conducted. Then, detached eddy simulation (DES) around 3D rotor blades is conducted. The results are compared with those of the experiment and the simulations on body-fitted grids.

The structure of this paper is as follows. Section 2 describes the numerical methods. In section 3, a 2D test problem is simulated to validate the proposed method. A 3D turbulent flow simulation of rotor blades is conducted to demonstrate the proposed approach in section 4. Finally, section 5 concludes this paper.

2. Numerical Methods

2.1 Cartesian grid generation

A quadtree (2D) or an octree (3D) structure is used for the staircase Cartesian grid generation around body surfaces. When one or more computer-aided design (CAD) data defines fluid regions and the interiors of bodies, UTCart can generate hierarchical Cartesian grids automatically. Figure 1 shows the technical terms used in this study. The cells are classified into two types, with the cells in the fluid region labeled “fluid cells,” and those that intersect with the body surface labeled “wall cells.” To determine the intersection of cells to input CAD data, the separating axis theorem is used [19]. The cell faces between the fluid and wall cells are “wall faces,” and fluid cells with wall faces are “the first cells.” Note that the cells completely inside the body are not used in this study.

As Fig. 1 shows, a staircase grid, which wall faces do not match the body surface, is generated. To generate the body-fitted grid, the first cells expand to body surfaces using simple projection strategies. The following section explains the details.

2.2 Recursive fitting method.

This section describes the RFM’s grid generation. 2D and 3D grids can be generated through the

same procedure. For simplicity, a 2D case is considered in the following explanation.

Figure 2a is the original Cartesian grid, while the first cells expand to the body surface using the closest points on the body surfaces to wall face vertices in Fig. 2b. The grid in the state shown in Fig. 2b is named the "initial RFM grid." Compared with the original Cartesian grid, the number of fluid cells does not change while the initial RFM grid has the additional fluid-fluid cell faces. Since the closest point on the body surface to an arbitrary point in the fluid region can be uniquely determined, the initial RFM grid generation is automatic and robust. In the initial RFM grid, one wall face consists of one line segment. To improve the shape reproducibility of the grid, additional points on the body surface are calculated. Then, the cell properties such as cell volume and cell centroid coordinates are modified. The grid shown in Fig. 2c is the "RFM grid." This modification is the key point of the RFM grid generation when the body surface comprises the geometric features, such as wing–fuselage junctures of the aircraft. Details of the RFM are explained in Refs [13,14]. Notably, the number of the fluid cells and cell faces is kept unchanged through cell property modification. Although flow around bodies with simple geometries, such as airfoil and rotor blades are calculated in this study, the grid of much more complex geometries can be automatically generated by the RFM.

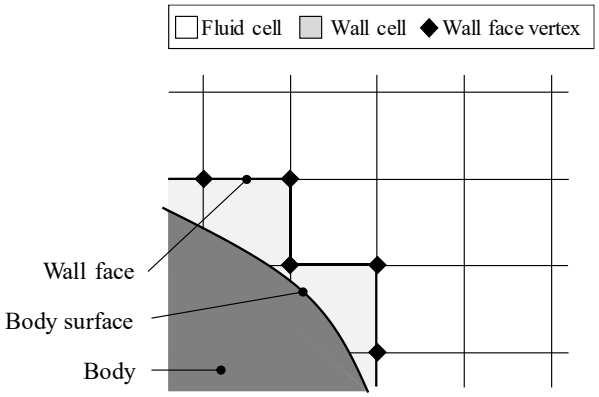

Figure 1 – Schematic of the Cartesian grid and definitions of the technical terms.

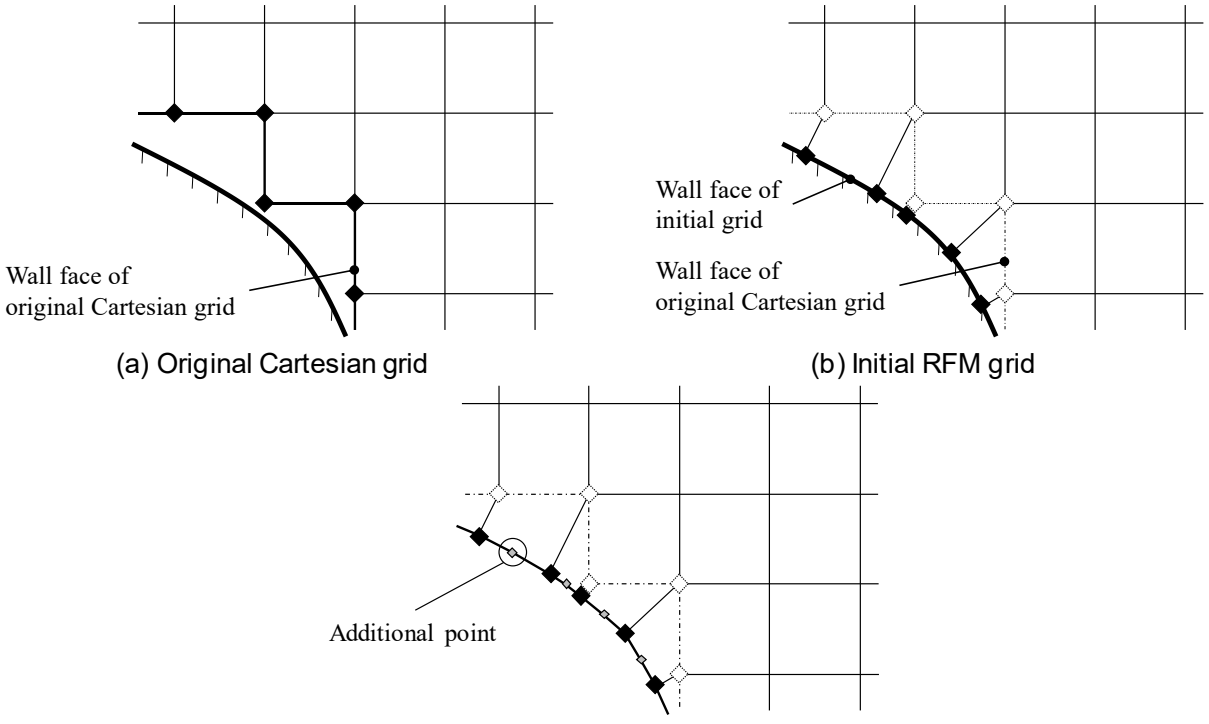

(a) Original Cartesian grid

(b) Initial RFM grid

(c) RFM grid

Figure 2 – RFM grid generation.

2.3 Flow simulation methods

The time-dependent Navier–Stokes equations for moving grids can be expressed in integral form as follows:

$$\frac{\partial}{\partial t}\iiint_V \boldsymbol{Q}_c dV + \iint_S \{(\boldsymbol{F}(\boldsymbol{Q}_c,\boldsymbol{n}) - \boldsymbol{Q}_c W_n) - \boldsymbol{F}_v\} dS = 0, \tag{1}$$

where the vector $\boldsymbol{Q}_c = [\rho, \rho u, \rho v, \rho w, E]^{\mathrm{T}}$ denotes conservative variables. The total energy E is equal to the sum of the internal energy ρe and the kinetic energy $\rho|\boldsymbol{u}|^2/2$. V denotes the control volume, S denotes the boundary of the control volume V, and vector $\boldsymbol{n} = [n_x, n_y, n_z]^{\mathrm{T}}$ is the outward-pointing unit normal vector to S. The vectors $\boldsymbol{F}$ and $\boldsymbol{F}_v$ are the inviscid and viscous flux, respectively. The scalar W_n denotes the normal component of the grid velocity to the control volume boundary, as

$$W_n = \boldsymbol{W} \cdot \boldsymbol{n}, \tag{2}$$

where $\boldsymbol{W} = [W_x, W_y, W_z]^{\mathrm{T}}$ is the velocity vector of the grid. In Eq. 1, the advection flux due to the grid motion $\boldsymbol{Q_c} W_{\boldsymbol{n}}$ is added to the Navier–Stokes equations for stationary grids. For a given problem, the simulation results should be identical when the velocity of the airflow relative to the grid velocity is the same, regardless of the grid motion. In this study, inviscid fluxes $\boldsymbol{F}$ and flux due to grid motion $\boldsymbol{Q_c} W_n$ are treated as one flux. Following the references [19,20], the matrix $\mathcal{T}_c$ is introduced as defined below:

$$\mathcal{T}_c = \begin{bmatrix} 1 & 0 & 0 & 0 & 0 \\ -W_x & 1 & 0 & 0 & 0 \\ -W_y & 0 & 1 & 0 & 0 \\ -W_z & 0 & 0 & 1 & 0 \\ \dfrac{|\boldsymbol{W}|^2}{2} & -W_x & -W_y & -W_z & 1 \end{bmatrix}. \tag{3}$$

Then, the fluxes are calculated as follows:

$$F(\boldsymbol{Q}_c, \boldsymbol{n}) - \boldsymbol{Q}_c W_n = \mathcal{T}_c^{-1} \boldsymbol{F}(\mathcal{T}_c \boldsymbol{Q}_c, \boldsymbol{n}), \tag{4}$$

$$\mathcal{T}_c \boldsymbol{Q}_c = \left[\rho, \rho(u - W_x), \rho\big(v - W_y\big), \rho(w - W_z), \rho e + \frac{\rho|\boldsymbol{u} - \boldsymbol{W}|}{2}\right]^{\mathrm{T}}. \tag{5}$$

In Eqs. 4 and 5, the vector $\mathcal{T}_c \boldsymbol{Q}_c$ denotes the conservative variables based on the relative velocity of the airflow to the control volume boundary. The vector $\mathcal{T}_c \boldsymbol{Q}_c$ is evaluated first. Then, the flux for the conservative variables $\boldsymbol{Q}_c$ is obtained via the inverse matrix $\mathcal{T}_c^{-1}$.

Equation 1 is discretized using the cell-centered finite volume method as follows:

$$\frac{\partial \boldsymbol{Q}_{c,i}}{\partial t} V_i + \sum_j \big(\mathcal{T}_p^{-1} \boldsymbol{F}_{ij}\big(\mathcal{T}_p \boldsymbol{Q}_{p,L}, \mathcal{T}_p \boldsymbol{Q}_{p,R}\big) - \boldsymbol{F}_{v,ij}\big) s_{ij} = 0, \tag{6}$$

$$\mathcal{T}_p = \begin{bmatrix} 1 & 0 & 0 & 0 & 0 \\ -\frac{W_x}{\rho} & 1 & 0 & 0 & 0 \\ -\frac{W_y}{\rho} & 0 & 1 & 0 & 0 \\ -\frac{W_z}{\rho} & 0 & 0 & 1 & 0 \\ 0 & 0 & 0 & 0 & 1 \end{bmatrix}, \tag{7}$$

where V_i is the cell volume of cell *i*, s_{ij} is the face area between cells *i* and *j*. The vectors $\boldsymbol{Q}_{p,L}$ and $\boldsymbol{Q}_{p,R}$ are the reconstructed primitive variables. The vector $\mathcal{T}_p\boldsymbol{Q}_p$ denotes the primate variables based on the relative velocity of the airflow to the cell face.

The approximate Riemann solver is used for the inviscid flux evaluation. In this study, the simple low-dissipation advection upstream splitting method (SLAU) is used [22]. When the relative velocity of airflow to the grid is transonic, Hishida's limiter is used to preserve monotonicity [23]. The viscous flux is evaluated by the second-order central difference. The unsteady flow problems are solved in time using the second-order backward difference with dual time stepping and Matrix-Free Gauss–Seidel implicit scheme (MFGS) [22]. Spalart–Allmaras (SA) one equation model [24] is used for 2D simulation, while the delayed detached eddy simulation-protected (DDES-p) [18,25] based on the SA model is used for 3D simulation. The DDES-p model introduces a simple modified shielding function to protect the RANS regions when the stream-wise grid size is small; thus, this model is suitable for unsteady flow simulations using Cartesian grids. To simulate the turbulent flow on moving Cartesian grids, the wall function is used to calculate the wall shear stress.

2.4 Implementation of wall function

In this study, the wall boundary conditions are the non-slip and adiabatic conditions; thus, the mass and heat fluxes through the wall face are strictly zero. The RFM grid does not comprise thin-layer cells near body surfaces. To accurately simulate the turbulent flow, the wall function is used to estimate the friction velocity u_τ and wall shear stress $\tau_{wall} = \rho_{wall}u_\tau^2$. Using the Newton–Raphson method, the friction velocity u_τ is iteratively calculated as follows:

$$u_\tau^{m+1} = u_\tau^m - \frac{g(u_\tau^m)}{g'(u_\tau^m)}, \tag{8}$$

$$g(u_\tau) = u_\tau f_{wall}(y^+) - \left(u_{t,1} - W_t\right), g'(u_\tau) = f_{wall}(y^+) + u_\tau\left\{\frac{\partial f_{wall}}{\partial u_\tau}(y^+)\right\}, \tag{9}$$

$$\frac{\partial f_{wall}}{\partial u_\tau} = \frac{\partial y^+}{\partial u_\tau}\frac{\partial f_{wall}}{\partial y^+} = \frac{y^+}{u_\tau}\frac{\partial f_{wall}}{\partial y^+}, \tag{10}$$

where the subscription 1 denotes the values of the first cell, f_{wall} is the SA wall function proposed by Allmaras et al. [26,27], $y^+ = y_1u_\tau/\nu_1$ is the dimensionless distance between the body surface and the first cell centroid. The tangential component of the grid velocity $W_t = \boldsymbol{W}\cdot\boldsymbol{t}$ becomes part of Eq. 9 to calculate the friction velocity. Further, the Crocco–Busemann relation [28] is employed to calculate the wall temperature, following the references. When IBMs are combined with wall functions, it has been reported that linearizing the tangential velocity profiles is crucial for the turbulent flow simulation. This is because the nonlinear velocity profiles cause an imbalance of the mass flux in the vicinity of the body surface [29,30]. Unlike the IBM simulation, the conservation laws are strictly satisfied in the RFM simulation. Therefore, the wall function used in this study is the original SA wall model assuming the near-wall velocity profiles to be nonlinear.

Figure 3 compares the point used for the friction velocity estimation based on the wall function. When combining Cartesian grid methods with wall functions, flow variables at the "image point" are widely used to calculate the friction velocity (Fig. 3a) [27,29,30]. Image points are set on the lines

perpendicular to the body surface. The distance between the body surface and image point d_{IP} is usually a constant parameter defined by the user, and the typical value of d_{IP} is two to three times the minimum grid size. Although turbulent boundary layers can be predicted on Cartesian grids by introducing the image point, the simulation result sometimes depends on the choice of d_{IP}. To avoid the dependence of the results on the user-specified parameter d_{IP}, the flow variables at the first cell centroid are used in this study (Fig. 3b). The distance between the body surface and first cell centroid d_1 is uniquely determined in each cell. As opposed to the simulation using image points, the distance between the body surface and the points used for the friction velocity estimation is not necessarily constant since cells with different shapes are generated around the body surface using the RFM. However, previous research shows that turbulent flow near the body surface can be predicted [13].

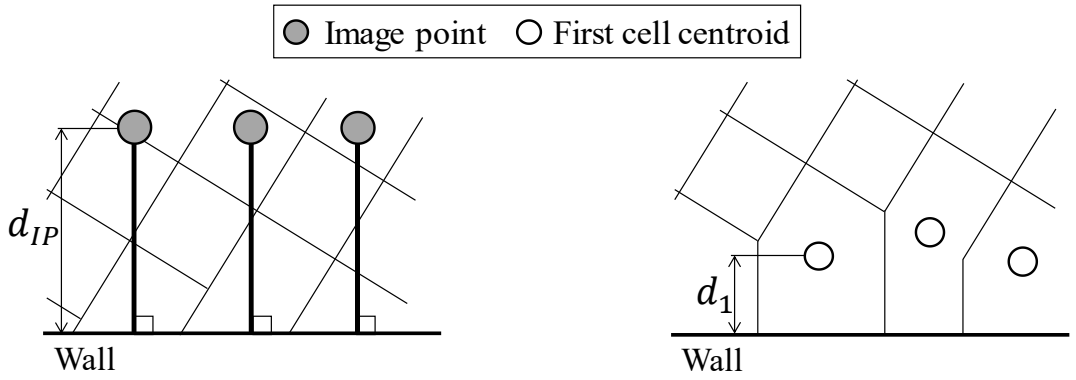

(a) Cartesian grid method with image point (b) Proposed method

Figure 3 – Comparison of the point used for the friction velocity estimation based on the wall function.

3. Two-dimensional flow of simulation

The unsteady RANS simulation of the pitching oscillating airfoil is conducted to demonstrate that unsteady aerodynamic characteristics can be predicted using the proposed method. The flow conditions and airfoil pitching motion are chosen to represent AGARD Case 3 [31]. The shape of an airfoil is NACA0012. The free-stream Mach number is $M_\infty = 0.6$, the Reynolds number based on the airfoil chord length c and free-stream velocity is $\mathrm{Re} = 4.8 \times 10^6$, and the center of rotation is 25% of the chord length. The angle-of-attack $\alpha(t)$ is described using the following expression:

$$\alpha(t) = \alpha_m + \alpha_0 \sin(\omega t), \tag{11}$$

where t denotes time, $\alpha_m = 4.86°$, and $\alpha_0 = 2.44°$. The reduced frequency is $k_r = (\omega c)/(2U_\infty) = 0.081$. To investigate the dependency of the simulation results on the grid size around an airfoil, three grids with different grid size is used. Table 1 summarizes the grid setting while Fig. 4 shows the computational grid around an airfoil. The grid represents the sharp corner of the trailing edge, as Fig. 4b shows. The dimensionless time step is $\Delta t = 0.08$, which corresponds to 800 steps/cycles. The initial conditions are steady-state solutions at $\alpha = \alpha_m$. The simulations are run over three cycles. The number of the inner sub-iterations for the dual time stepping is 50. The simulation on the RFM grid is compared with those on conventional body-fitted grids in Refs. [32,33]. One reference simulation is conducted by Biedron et al. using FUN3D [7], and the other simulation is conducted by Takahashi et al. using TAS [32].

Figure 5 shows the pressure distribution as the airfoil pitches up at $\alpha = 5.92°$, and shock is observed on the upper surface. Figure 6 shows the dependency of unsteady aerodynamics prediction on the grid size. In all simulations, lift and pitching moment coefficients are the same when the airfoil pitches up. By contrast, compared with Grid 2 and 3, the lift coefficient is underestimated while the pitching moment coefficient is overestimated in Grid 1 simulation when the airfoil pitch downs. Figure 7 shows Mach number distributions and streamlines when the airfoil pitches down.

The flow separates around the trailing edge in Grid 1 simulation. As Fig. 6 shows, almost the same unsteady aerodynamic forces are predicted in Grid 2 and 3 simulations. Therefore, the results of Grid 2 are compared with the reference simulations on conventional body-fitted grids. As Fig. 8a shows, a hysteresis loop is observed, i.e., the lift coefficient depends on whether the angle-of-attack increases or decreases for a given angle. The inversion of the lift coefficient trajectory at $\alpha \sim 6°$ is observed in the RFM simulation, with the inversion found to be consistent with the experiment. Further, the result of the RFM simulation agrees with those of TAS and FUN3D simulations on body-fitted grids. Figure 8b shows the pitching moment coefficient vs. angle-of-attack. The result of the RFM simulation is almost the same as those of the experiment and the FUN3D simulation. As above, the unsteady aerodynamics predicted by the RFM are in good agreement with those of the wind tunnel test and the reference simulations on conventional body-fitted grids. The dependency on the angle-of-attack and the hysteresis loop of the aerodynamic coefficients are also predicted by the RFM.

Table 1 – Grid settings (AGARD problem).

	Grid 1	Grid 2	Grid 3
Grid size around airfoil $\Delta x/c$	2.50×10^{-4}	1.25×10^{-4}	6.25×10^{-5}
Total cell number	84,542	164,798	326,392
y^+ at $x/c \sim 0.5$	Approx. 40	Approx. 20	Approx. 10

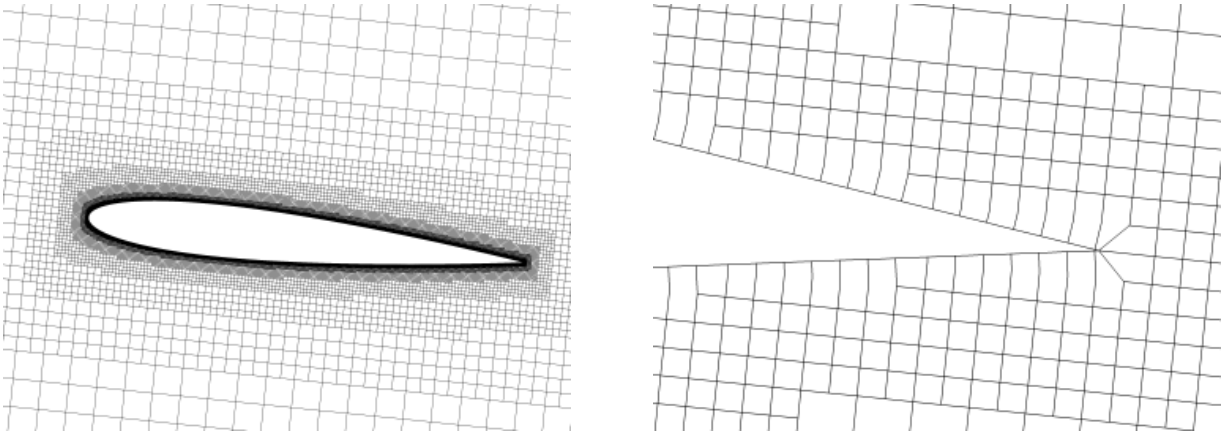

(a) Overall (b) Close-up view around trailing edge

Figure 4 – Computational grid (Grid2).

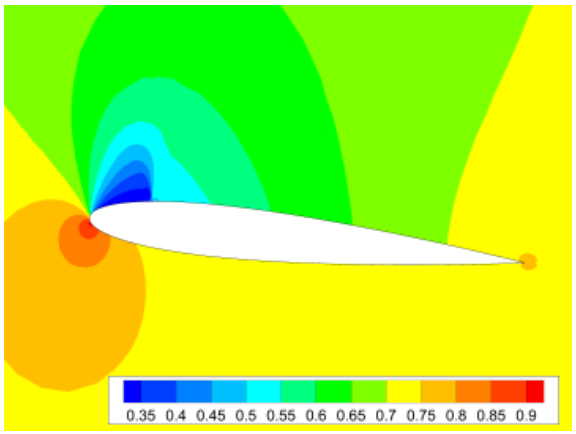

Figure 5 – Pressure distribution as the airfoil pitched up ($\alpha = 5.92°$, Grid2).

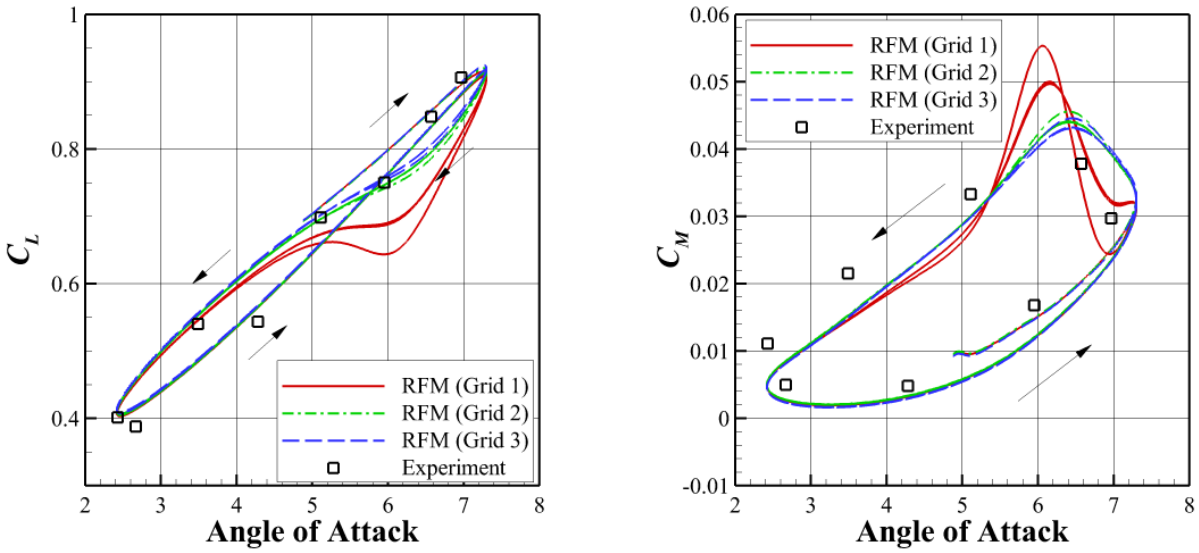

(a) Lift coefficient vs. angle of attack (b) Pitching moment coefficient vs. angle of attack

Figure 6 – Effect of grid refinement on unsteady aerodynamics prediction.

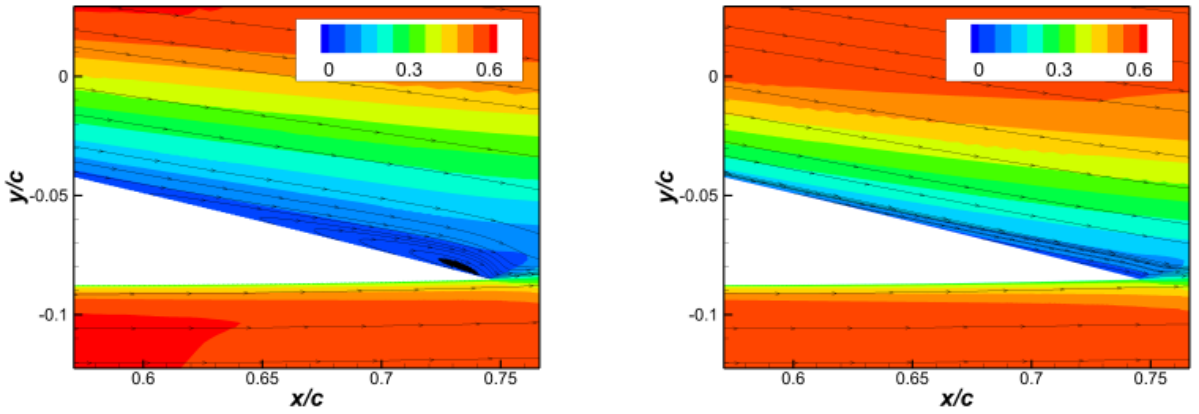

(a) Grid 1 (b) Grid 2

Figure 7 – Comparison of Mach number distributions and streamlines at $\alpha = 6.52°$ (pitch-down).

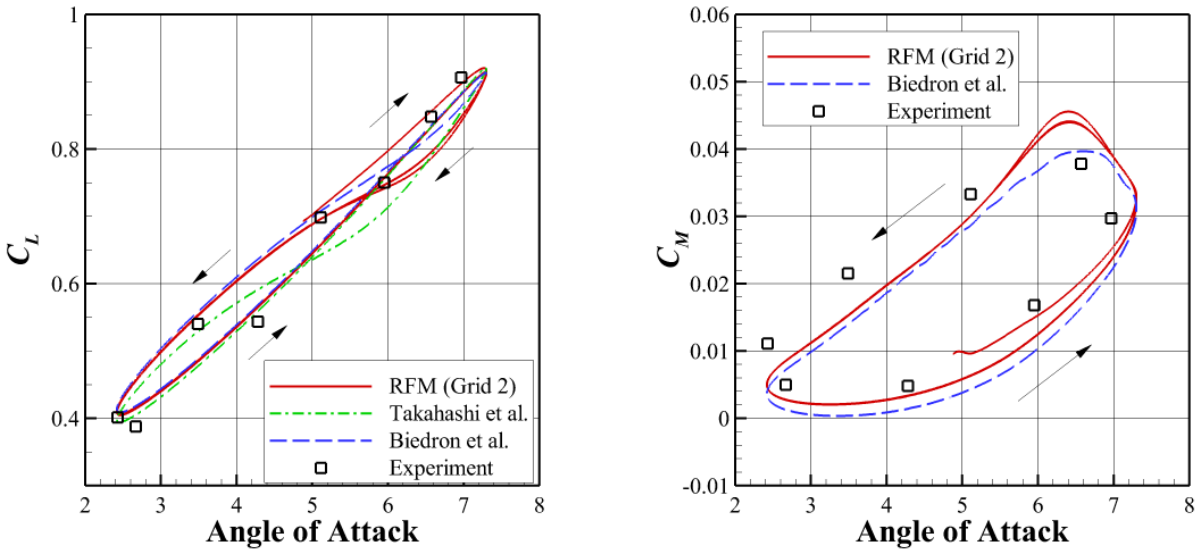

(a) Lift coefficient vs. angle of attack (b) Pitching moment coefficient vs. angle of attack

Figure 8 – Comparison of predicted unsteady aerodynamics with reference simulations on conventional body-fitted grids.

4. Three-dimensional Turbulent Flow Simulation of Rotor Blade

4.1 Problem definition

To investigate the capacity of the proposed method to predict the unsteady aerodynamics of 3D moving bodies, unsteady turbulent flow simulations of the rotor in hover conditions are conducted. The conditions are the same as the experimental tests conducted by Caradonna and Tung [33]. Table 2 summarizes the geometric parameters and flow conditions. In this study, the tip Mach number is $M_{tip} = \Omega R/a_\infty = 0.439$ and 0.890, where Ω and R are the angular velocity and rotor radius, respectively. The collective pitch angle is $\theta = 8°$. Note that the boundary layers on the rotor blades are assumed to be fully turbulent in the simulation.

4.2 Grid setting

Figure 9 and Table 3 show the grid settings. The airflow speed relative to the blade increases from the blade root to the blade tip. Accordingly, the Reynolds number based on the relative airflow speed increases; therefore, the cells around the blade tip are refined. The grid size at the blade tip is $\Delta x/C = 1/500$. To accurately predict the flow in the wake region, the grid is uniformly refined, as Fig. 9b shows. Note that the shape of the uniformly refined region is cuboid. Figure 10 shows the distribution of dimensionless wall distance at the first cells. The dimensional wall distance y^+ is about 100 on the upper surface of the blades when the tip Mach number is $M_{tip} = 0.439$.

Table 2 – Rotor properties and flow conditions.

Number of blades	2
Rotor radius R	45 [in.]
Chord length C	7.5 [in.]
Airfoil	NACA0012
Temperature of air	288 [K]
Collective pitch angle θ_c	8 [deg]
Revolutions per minute	1,250 and 2,540
Tip Mach number	0.439 and 0.890
Reynolds number based on the chord length and the sonic speed	4.44×10^6

Table 3 – Grid settings for rotor simulation.

Grid size (blade root side)	3.00×10^{-2} [in.]
Grid size (blade tip side)	1.50×10^{-2} [in.]
Grid size (wake)	2.40×10^{-1} [in.]
Total cell number	76,141,294

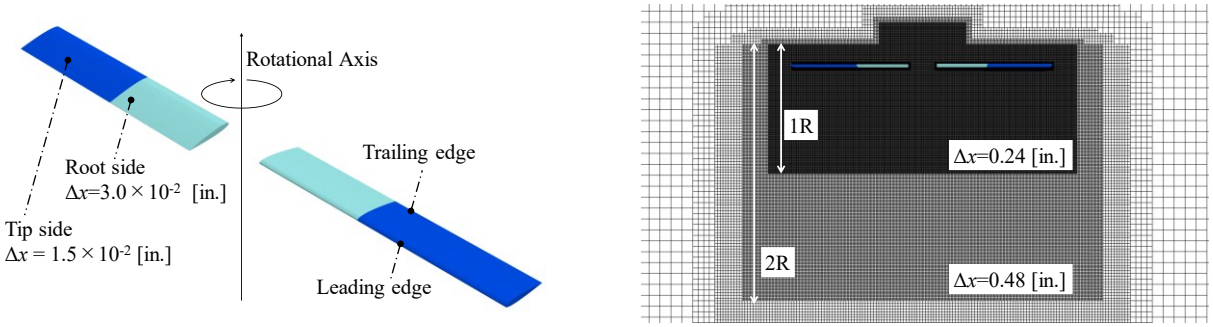

(a) Grid size around rotor blades (b) Grid size in uniform refined region

Figure 9 – Grid settings of Caradonna–Tung rotor problem.

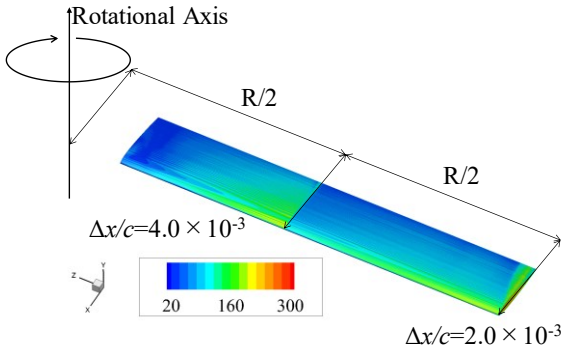

Figure 10 – Dimensionless distance distribution ($M_{tip} = 0.439$).

4.3 Solution approach

In this problem, the unsteady flow around rotor blades is simulated using DDES-p. To predict unsteady aerodynamics, it is crucial to accurately simulate the unsteady flow at the rotor wake region. Besides, from the viewpoint of post-processing, it is convenient that the simulation steps for both cases are the same. In this study, the dimensionless time step is $\Delta t = 0.179$ for $M_{tip} = 0.439$ and $\Delta t = 0.0882$ for $M_{tip} = 0.890$, corresponding to 3,600 steps/revolutions for both cases. With these values, the Courant number based on the sonic speed and blade tip velocity is approximately 1 at the rotor wake. When $M_{tip} = 0.890$, the shock wave appears around rotor tips; thus, the limiter for inviscid flux evaluation is used to preserve monotonicity.

Figure 11a shows the history of the thrust coefficients C_T. Based on the findings in Refs. [10,34], the first 10 revolutions are calculated using two sub-iterations ((1) in Fig. 11a). Here, the aim is not to obtain accurate solutions but to quickly remove any initial transients. Following this, the number of sub-iterations increases to 10. In this simulation, the inner residual drops one order of magnitude after the inner sub-iterations. Although the number of sub-iterations for implicit time integration is an open issue for unsteady simulations, a one-order-of-magnitude reduction of the inner residual is widely used as a convergence criterion, and such a reduction is sufficient for yielding good results, as demonstrated in Refs [8,35]. The simulations are run over 12 rotor revolutions ((2) and (3) in Fig. 11a), with the time-averaged values calculated using the data of the last four rotations ((3) in Fig. 11a).

The flow simulations are performed on Fujitsu PRIMERGY CX400M1/CX2550M5 system (Oakbridge-CX) at the University of Tokyo using 896 cores with Message Passing Interface (MPI) parallelization [36]. The wall-clock time for 22 revolutions is 88 hours when $M_{tip} = 0.439$, while 96 hours are required when $M_{tip} = 0.890$. Since the limiter is used for inviscid flux evaluation when $M_{tip} = 0.890$, the computational cost increases.

4.4 Results

Figures 11a and b show the histories of thrust coefficients (C_T) and Figure of Merit (FM). Although C_T and FM histories oscillate, the last four revolutions are in quasi-steady states. Table 4 shows comparisons of the time-averaged C_T and FM values. When the tip Mach number increases, the thrust coefficients increase while the Figure of Merit decreases. As the reference [33] shows, C_T also increases in the experiment. It seems that the FM decreases due to the wave drag at blade tips. Meanwhile, Figs. 12 and 13 show comparisons of the time-averaged blade surface pressure coefficient C_p distributions at three sections $r/R = 0.50, 0.80, 0.96$. The results of the RFM simulation agree with the experimental data. As Fig. 12 shows, it is observed that the suction peak increases from the blade root to the blade tip in the experimental data when the tip Mach number is $M_{tip} = 0.439$. The same trend is observed in the RFM simulation. Further, discontinuous changes of C_p due to the shock wave are observed when the tip Mach number is $M_{tip} = 0.890$, as Fig. 13 shows. Figure 14 shows the iso-surface of the Q criterion colored by the velocity along the rotational axis at 22 revolutions, with the helical blade tip vortices being observed. As discussed above, although the proposed approach can generate the body-fitted Cartesian grid automatically, the results of flow simulation are in good agreement with the results of the experimental data. This is advantageous over the simulation on conventional body-fitted structured/unstructured grids in terms of grid generation.

Table 4 – Comparison of the thrust coefficients and Figure of Merit values.

Tip Mach number	Thrust coefficient	Figure of Merit
0.439	0.00516	0.543
0.890	0.00577	0.457

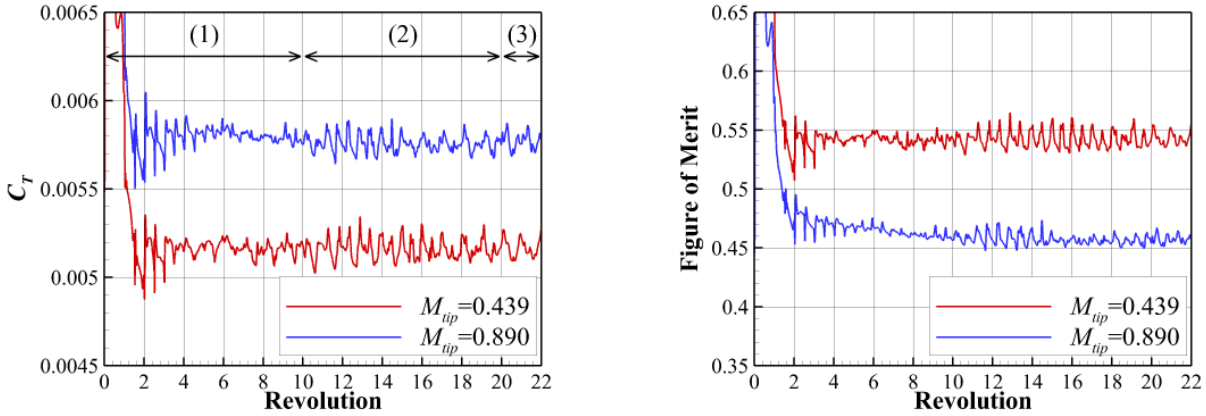

(a) Thrust coefficients (b) Figure of Merit

Figure 11 – Histories of predicted rotor aerodynamics.

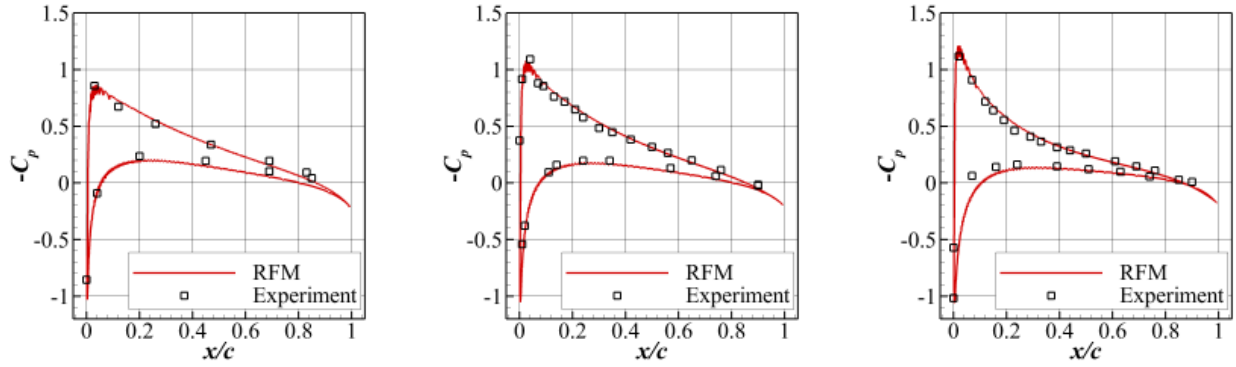

(a) $r/R = 0.50$ (b) $r/R = 0.80$ (c) $r/R = 0.96$

Figure 12 – Surface pressure coefficient distributions ($M_{tip} = 0.44$).

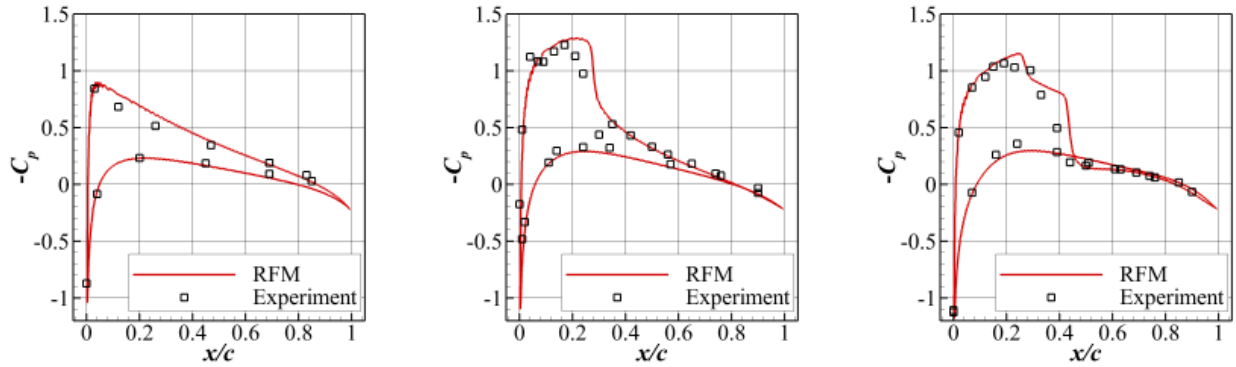

(a) $r/R = 0.50$ (b) $r/R = 0.80$ (c) $r/R = 0.96$

Figure 13 – Surface pressure coefficient distributions ($M_{tip} = 0.89$).

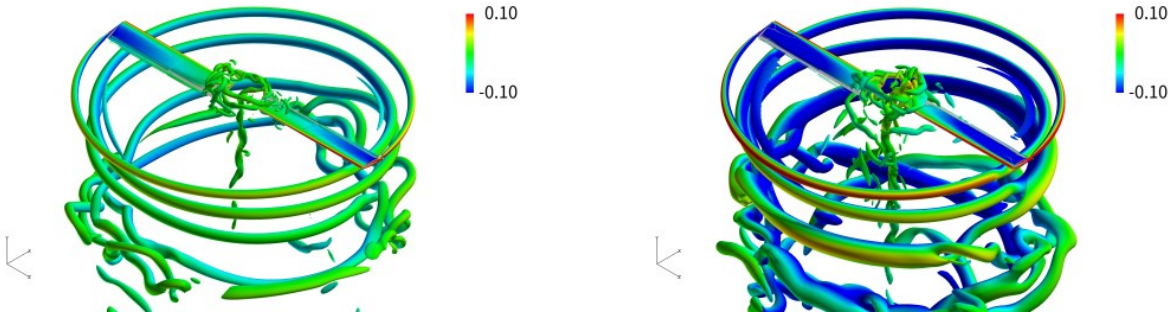

(a) $M_{tip} = 0.439$ (b) $M_{tip} = 0.890$

Figure 14 – Iso-surface of the Q criterion colored by the velocity along the rotational axis.

5. Conclusions

In this study, a new method capable of automatic grid generation and accurate turbulent flow simulation around 2D and 3D moving bodies was proposed. The RFM based on the Cartesian grid method was used to generate the body-fitted grid automatically, while the body motion was simulated using the moving grid method. Since the automatically generated body-fitted Cartesian grid was used, near-wall treatment became straightforward in flow simulation compared with IBMs. To examine the capability of the proposed method, 2D and 3D unsteady turbulent flow was simulated. To examine the capacity of the proposed method, a 2D RANS simulation of the pitching airfoil and a 3D DES simulation of the rotor blades was conducted. 3D simulations were performed on the supercomputer system at the University of Tokyo. The results showed that the RFM simulations were in good agreement with the results of the experimental tests and the simulations on conventional body-fitted grids.

Acknowledgements

This research is partially supported by Initiative on Promotion of Supercomputing for Young or Women Researchers, Supercomputing Division, Information Technology Center, The University of Tokyo. The images in this paper were created using FieldView, as provided by Intelligent Light through its University Partner Program.

Copyright Statement

Contact Author Email Address

sugaya.keisuke@jaxa.jp (Keisuke Sugaya)

References

[1] Brelje, B. J., Martins, J. R. R. A., "Electric, hybrid, and turbo electric fixed wing aircraft: A review of concepts, models, and design approaches," *Progress in Aerospace Science*, Vol. 104, 2019, pp. 1–19. https://doi.org/10.1016/j.paerosci.2018.06.004

[2] Mittal, R., and Iaccarino, G., "IMMERSED BOUNDARY METHODS," *Annual Review of Fluid Mechanics*, Vol. 37, No. 1, 2005, pp. 239–261.
http://doi.org/10.1146/annurev.fluid.37.061903.175743

[3] Seo, J. H., and Mittal, R., "A sharp-interface immersed boundary method with improved mass conservation and reduced spurious pressure oscillations," *Journal of Computational Physics*, Vol. 230, Issue 19, 2011, pp. 7347–7363.
https://doi.org/10.1016/j.jcp.2011.06.003

[4] Lee, J., Kim, J., Choi, H., and Yang, K.-S., "Sources of spurious force oscillations from an immersed boundary method for moving-body problems," *Journal of Computational Physics*, Vol. 230, No. 7, 2011, pp. 2677–2695.
https://doi.org/10.1016/j.jcp.2011.01.004

[5] Borker, R., Huang, D., Grimberg, S., Farhat, C., Avery, P., and Rabinovitch, J., "Mesh adaptation framework for embedded boundary methods for computational fluid dynamics and fluid‐structure interaction," *International Journal for Numerical Methods in Fluids*, Vol. 90, Issue 8, 2019, pp. 389–424.
https://doi.org/10.1002/fld.4728

[6] Lahur, P. R., and Nakamura, Y., "Flow Calculation of Moving Body on Cartesian Grid by Using New Cell-Merging Method," *Transactions of the Japan society for aeronautical and space sciences*, Vol 44, Issue, 145, 2001, pp. 171–178.
https://doi.org/10.2322/tjsass.44.171

[7] Biedron, R. T., Vatsa, V. N., and Atkins, H. L., "Simulation of Unsteady Flows Using an Unstructured Navier-Stokes Solver on Moving and Stationary Grids," 23rd AIAA Applied Aerodynamics Conference, AIAA Paper 2005-5093, June 2005.
https://doi.org/10.2514/6.2005-5093

[8] Yu, M. and Wang, L., "A high-order flux reconstruction/correction procedure via reconstruction formulation for unsteady incompressible flow on unstructured moving grids," *Computers & Fluids*, Vol. 139, 2016, pp. 161–173.
https://doi.org/10.1016/j.compfluid.2016.05.028

[9] Posa, A., and Broglia, R., "An immersed boundary method coupled with a dynamic overlapping-grids strategy," *Computers & Fluids,* Vol. 191, 2019, Article No. 104250.
https://doi.org/10.1016/j.compfluid.2019.104250

[10] Sugaya, K., and Imamura, T., "Unsteady turbulent flow simulations on moving Cartesian grids using immersed boundary method and high-order scheme," *Computers & Fluids*, Vol. 231, 2021, Article No. 105173.
https://doi.org/10.1016/j.compfluid.2021.105173

[11] Osher, S. and Sethian, J., "Fronts propagating with curvature-dependent speed: Algorithms based on Hamilton-Jacobi formulations," *Journal of Computational Physics*, Vol. 79, No. 1, 1988, pp. 12 – 49.
http://doi.org/10.1016/0021-9991(88)90002-2.

[12] Wang, Z. J., and Srinivasan, K., "An adaptive Cartesian grid generation method for 'Dirty' geometry," *International Journal for Numerical Methods in Fluids*, Vol. 39, Issue 8, 2002, pp. 703–717.
https://doi.org/10.1002/fld.344

[13] Sugaya, K., and Imamura, T., "Aerodynamic Analysis of Common Research Model at Low Speed Conditions Using Recursive Fitting Method and Wall Function," AIAA Scitech 2022 Forum, AIAA Paper 2022-0448, January 2022.
https://doi.org/10.2514/6.2022-0448

[14] Sugaya, K., and Imamura, T., "A Recursive Fitting Approach for Automatic Grid Generation Around Aircraft Configuration," *Journal of the Japan Society for Aeronautical and Space Sciences*, Vol. 68, No. 3, 2020, pp. 115–122 (in Japanese).
https://doi.org/10.2322/jjsass.68.115

[15] Harada, M., Tamaki, Y., Takahashi, Y., and Imamura, T., "A Novel Simple Cut-Cell Method for Robust Flow Simulation on Cartesian Grids," 54th AIAA Aerospace Sciences Meeting, AIAA Paper 2016-0601, January 2016.
https://doi.org/10.2514/6.2016-0601

[16] Harada, M., Tamaki, Y., Takahashi, Y., and Imamura, T., "Simple and Robust Cut-Cell Method for High-Reynolds-Number-Flow Simulation on Cartesian Grids," *AIAA Journal*, Vol. 55, No. 8, 2017, pp. 2833–2841.
https://doi.org/10.2514/1.J055343

[17] Tamaki, Y., and Imamura, T., "Turbulent Flow Simulations of the Common Research Model Using Immersed Boundary Method," *AIAA Journal*, Vol. 56, No. 6, 2018, pp. 2271–2282.
https://doi.org/10.2514/1.J056654

[18] Imamura, T., and Tamaki, Y., "Unsteady Flow Simulation Around Two-Wheel Main Landing Gear Based on Compressible Navier-Stokes Solver with Immersed Boundary Method," AIAA AVIATION 2020 FORUM, AIAA Paper 2020-2579, June 2020.
https://doi.org/10.2514/6.2020-2579

[19] Akenine-Möller, T., "Fast 3D Triangle-Box Overlap Testing," ACM SIGGRAPH 2005 Courses, SIGGRAPH '05, Association for Computing Machinery, New York, NY, USA, 2005,
https://doi.org/10.1145/1198555.1198747.

[20] Muffo, D., Quaranta, G., Guardone, A., and Mantegazza, P., "Interface Velocity Consistency in time-accurate flow simulations on dynamic meshes," Scientific Report DIA-SR 07-01, Politecnico di Milano, 2007.

[21] Nishikawa, H., "Roe Flux in Deforming Mesh," Web-published note.
http://doi.org/10.13140/RG.2.2.20266.57288

[22] Shima, E. and Kitamura, K., "Parameter-Free Simple Low-Dissipation AUSM-Family Scheme for All Speeds," *AIAA Journal*, Vol. 49, No. 8, 2011, pp. 1693–1709.
http://doi.org/10.2514/1.J050905

[23] Hishida, M., Hashimoto, A., Murakami, K., and Aoyama, T., "A new slope limiter for fast unstructured CFD solver FaSTAR," JAXA Special Publication: Proceedings of 42nd Fluid Dynamics Conference / Aerospace Numerical Simulation Symposium 2010, JAXA, February 2011, pp. 85–90, JAXA-SP-10-012 (in Japanese).
http://id.nii.ac.jp/1696/00004716/

[24] Spalart, P. R. and Allmaras, S., "A one-equation turbulence model for aerodynamic flows," 30th Aerospace Sciences Meeting and Exhibit, AIAA Paper 92-0439, January 1992.
http://doi.org/10.2514/6.1992-439

[25] Tamaki, Y., Imamura, T., and Kawai, S., "Effect of the Boundary-Layer Shielding Function on Delayed Detached-Eddy Simulation of Transonic Buffet," Annual Meeting of the Japan Society of Aeronautical and Space Sciences, 2018 (in Japanese).

[26] Allmaras, S., Johnson, F., and Spalart, P., "Modifications and clarifications for the implementation of the Spalart-Allmaras turbulence model," Seventh International Conference on Computational Fluid Dynamics (ICCFD7), 2012.

[27] Berger, M. and Aftosmis, M. J., "Progress Towards a Cartesian Cut-Cell Method for Viscous Compressible Flow," 50th AIAA Aerospace Sciences Meeting including the New Horizons Forum and Aerospace Exposition, Aerospace Sciences Meetings, 2011, AIAA Paper 2012-1303, January 2013.
https://doi.org/10.2514/6.2012-1301

[28] White, F. M., Viscous Fluid Flow, McGraw - Hill, New York, 1974, pp. 578-581, 627-629.

[29] Capizzano, F., "Turbulent Wall Model for Immersed Boundary Methods," *AIAA Journal*, Vol. 49, No. 11, 2011, pp. 2367–2381.
https://doi.org/10.2514/1.J050466

[30] Tamaki, Y., Harada, M., and Imamura, T., "Near-Wall Modification of Spalart–Allmaras Turbulence Model for Immersed Boundary Method," *AIAA Journal*, Vol. 55, No. 9, 2017, pp. 3027–3039.
https://doi.org/10.2514/1.J055824

[31] Landon, R. H., "NACA0012 Oscillation and Transient Pitching, Compendium of Unsteady Aerodynamic Measurements," AGARD Report 702, Data set 3, 1983.
https://doi.org/10.2514/6.2009-1360

[32] Takahashi, S., Monjugawa, I., and Nakahashi, K., "Unsteady Flow Computations around Moving Airfoils

by Overset Unstructured Grid Method," *Transactions of the Japan Society for Aeronautical and Space Sciences*, Vol. 51, No. 172, 2008, pp. 78–85,
https://doi.org/10.2322/tjsass.51.78.

[33] Caradonna, F. X. and Tung, C., "Experimental and analytical studies of a model helicopter rotor in hover," Conference Paper NASA-TM-81232, NASA, September 1981.
https://ntrs.nasa.gov/search.jsp?R=19820004169

[34] Coder, J. G., "OVERFLOW Rotor Simulations Using Advanced Turbulence and Transition Modeling," 55th AIAA Aerospace Sciences Meeting, AIAA Paper 2017-1432, January 2017.
https://doi.org/10.2514/6.2017-1432

[35] Lakshminarayan, V., Sitaraman, J., and Wissink, A, "Sensitivity of rotorcraft hover predictions to mesh resolution in strand grid framework." *AIAA Journal*, Vol. 57, No. 8, 2019, pp. 3173–3184.
https://doi.org/10.2514/1.J056571

[36] Oakbridge-CX supercomputer system | supercomputing division, Information Technology Center, The University of Tokyo, https://www.cc.u-tokyo.ac.jp/en/supercomputer/obcx/service/ [Retrieved on Feb.24th, 2022].